Methods

Modelling of continental corner collision

Modelling approach

The geodynamic, fully coupled, three-dimensional, thermo-mechanical-surface-process C code I3VIS-FDSPM combines a finite-difference method with a marker-in-cell technique on a staggered Eulerian grid [1–3]. The code solves the conservation of momentum, mass and energy equations on the Eulerian grid, while rock units – markers – are advected through the fixed Eulerian grid following the velocity field interpolated from the surrounding fixed grid points. The rocks deform following non-Newtonian visco-plastic rheologies (Extended Data Table 1). The code takes into account frictional, adiabatic, and radiogenic heat production. The complete description is provided in previous works[1,2].

Numerical model design

The models consist of 501 x 501 x 101 (X, Z, Y) Eulerian nodes with a uniform 2 km grid step in each direction, corresponding to a model domain size of 1000 x 1000 x 200 km. Each cell contains two markers in each direction. The model domain is resolved using 25 million Eulerian nodes through which 200 million markers advect the rock properties. The reference model consists of four continental plates: the indenter, representing part of India, is located in the southwest corner and transitions into the slightly weaker Eurasian plate to the north and east (Extended Data Fig. 1A). To mimic the effects of the cratonic Tarim and Sichuan basins, we use a northern and eastern strong zone (NSZ and ESZ). The Indian indenter (Eurasian) plate consists of 20 (23) wet quartzite upper crust, 15 (17) km wet plagioclase lower crust, and 105 (80) km of lithospheric mantle (Extended Data Fig. 1, Extended Data Table 1). The NSZ and ESZ have the same crustal thicknesses as the indenter, but thicker lithospheric mantles of 125 and 145 km, respectively. This makes them significantly colder and therefore stronger than the other plates (Extended Data Fig. 1B). To initiate subduction and to ensure that India is the lower plate in each direction, two weak zones composed of serpentinised mantle are emplaced between the indenter and Eurasia towards the north and towards the East. They extend from the base of the crust to the base of the lithospheric mantle at an angle of 30° (Extended Data Fig. 1A) and represent the Tethys suture and Burmese subduction zone. In front of the indenter and within the Eurasian domain, a proto-plateau is defined between X = 0-400 km and Z = 340-740 km, which has a 35 km thick upper crust, 10 km lower crust, and 75 km of lithospheric mantle. The effect of this proto-plateau is discussed in the main text. Finally, we use a 20 km thick layer of sticky air to allow topography to build up (Extended Data Table 1).

The indenter initially has a 3-segment geotherm (300°C at the mid-crust interface, 400°C at the Moho), while Eurasia (500°C at the Moho) and the proto-plateau (600°C at the Moho) have a 2-segment geotherm. The strong zones have an initial linear geotherm from 0°C at the surface to 1350°C at the lithosphere-asthenosphere boundary (LAB), which is the same temperature for all plates. An adiabatic gradient of 0.5°C/km is applied in the asthenospheric mantle. The model sides are insulating, i.e. zero horizontal heat flux. An infinity-like external temperature is prescribed at the lower boundary, implying a temperature of 1216°C at Y = 400 km. Therefore, the temperature and vertical heat flux at the resolved lower boundary can vary[4–6]. Similarly, we impose an external free slip boundary condition at Y = 400 km allowing for subduction through the lower boundary despite our limited vertical model extent. The side and back boundaries are free slip. We apply a push velocity of 5 cm/yr to the Indian indenter, which tapers to 0 cm/yr between X = 400-500 km (Extended Data Fig. 1A). The material

influx is compensated with an outflux of air at the top of the model domain of 0.041 cm/yr and an outflow of mantle through the lower boundary of 0.85 cm/yr to conserve volume.

Extended Data Table 1| Rheological parameters for the reference model. All units displayed here have a specific heat capacity of 1000 J kg^{-1} K^{-1}. Sticky air has a density of 1 kg m^{-3} and a constant viscosity of 10^{-18} Pa s.

	Sediments[7]	Upper cont. Crust[7]	Lower cont. Crust[7]	Lithospheric mantle[8]	Asthenospheric mantle[8]	Mantle weak zone[9]
Flow law	Wet qtz.	Wet qtz.	Plag.	Dry olivine	Dry olivine	Wet olivine
Density ρ_0 [kg m^{-3}]	2600	2700	2800	3300	3300	3300
Pre-exponential factor, $\frac{1}{A_D}$ [Pa^n s^{-1}]	$1.97 \cdot 10^{17}$	$1.97 \cdot 10^{17}$	$4.8 \cdot 10^{22}$	$1.10 \cdot 10^{16}$	$1.10 \cdot 10^{16}$	$1.10 \cdot 10^{16}$
Activation energy, E [kJ mol^{-1}]	154	154	238	530	530	530
Activation volume, V [J bar^{-1}]	0	0	0	2.6	2.6	2.6
Stress exponent n	2.3	2.3	3.2	3.5	3.5	3.5
Cohesion [MPa]	1	1	1	3	3	3
Friction coefficient range $[\mu_0, \mu_1]$	[0,0]	[0.2, 0.1]	[0.2, 0.1]	[0.6, 0.0]	[0.6, 0.0]	[0, 0]
Strain weakening interval $[\varepsilon_0, \varepsilon_1]$	[0.5, 1.5]	[0.25, 1.0]	[0.25, 1.0]	[0, 0.5]	[0, 0.5]	[0, 0.5]
Radioactive heat production H_r [μW m^{-3}]	2	1	0.5	0.022	0.024	0.026
Thermal expansivity α [$°K^{-1}$]	$3 \cdot 10^{-5}$	$3 \cdot 10^{-5}$	$3 \cdot 10^{-5}$	$2 \cdot 10^{-5}$	$2 \cdot 10^{-5}$	$2 \cdot 10^{-5}$
Compressibility coefficient [$kbar^{-1}$]	$1 \cdot 10^{-3}$	$1 \cdot 10^{-3}$	$1 \cdot 10^{-3}$	$6 \cdot 10^{-4}$	$6 \cdot 10^{-4}$	$6 \cdot 10^{-4}$
Thermal conductivity k [W $m^{-1}K^{-1}$]	$\left(0.64 + \frac{807}{T+77}\right)\exp(4 \cdot 10^{-6}P)$	$\left(0.64 + \frac{807}{T+77}\right)\exp(4 \cdot 10^{-6}P)$	$\left(1.18 + \frac{474}{T+77}\right)\exp(4 \cdot 10^{-6}P)$	$\left(0.73 + \frac{1293}{T+77}\right)\exp(4 \cdot 10^{-6}P)$	$\left(0.73 + \frac{1293}{T+77}\right)\exp(4 \cdot 10^{-6}P)$	$\left(0.73 + \frac{1293}{T+77}\right)\exp(4 \cdot 10^{-6}P)$

Visco-plastic rheological model

We use an effective viscosity formulation to simulate the plastic ("brittle") and viscous (ductile) strength of the modelled rocks, using the properties in Extended Data Table 1. The viscous flow laws for dislocation and diffusion creep are harmonically averaged into a ductile viscosity η_{ductile}

$$\frac{1}{\eta_{\text{ductile}}} = \frac{1}{\eta_{\text{newt}}} + \frac{1}{\eta_{\text{powl}}}$$

Here, η_{newt} and η_{powl} represent the contributions from diffusion and dislocation creep. For the crust and sediments, these are calculated as

$$\eta_{\text{newt}} = \frac{A_{\text{d}}}{2\sigma_{\text{cr}}^{n-1}} \exp\left(\frac{E_{\text{a}} + PV_{\text{a}}}{RT}\right)$$

$$\eta_{\text{powl}} = \frac{A_d^{1/n}}{2} \exp\left(\frac{E_a + PV_a}{nRT}\right) \dot{\varepsilon}_{\text{II}}^{\frac{1}{n-1}}$$

Where A_{d} is the prefactor for both creep laws, σ_{cr} defines the transition stress between diffusion and dislocation creep, E_{a} and V_{a} represent the activation energy and volume, n is the stress exponent, and R and T are the universal gas constant and absolute temperature. $\dot{\varepsilon}_{\text{II}}$ is the second invariant of the strain rate tensor. A_{d}, E_{a}, V_{a}, and n are determined from experiments.

For mantle rocks, a different diffusion creep flow law is used, now also considering grain size evolution

$$\eta_{\mathrm{newt,mantle}} = \frac{A_{\mathrm{d,GSE}}}{2}\exp\left(\frac{E_{\mathrm{a}} + PV_{\mathrm{a}}}{RT}\right)\left(\frac{\pi \mathrm{r}}{2}\right)^{m}$$

Here, $A_{\mathrm{d,GSE}}$ now depends on the deformation regime, r is the grain interface curvature and m the grain size exponent. The curvature is coupled to the actual grain size through the factor $(\pi/2)$[10].

After calculating the ductile rheology, it is merged with the brittle part to obtain an effective visco-plastic rheology as follows:

$$\eta_{\mathrm{ductile}} \leq \frac{C + \mu(\varepsilon)P}{2\dot{\varepsilon}_{\mathrm{II}}},$$

Here, C is the tensile strength of rocks at zero pressure, P is pressure, $\dot{\varepsilon}_{\mathrm{II}} = \sqrt{(\dot{\varepsilon}_{\mathrm{ij}}\dot{\varepsilon}_{\mathrm{ij}})/2}$ is the second invariant of the strain rate tensor, and μ is the friction angle that decreases over a predefined interval of accumulated plastic strain $\varepsilon_{\mathrm{pl}}$ from the static friction coefficient μ_0 to the weakened value μ_1 (Extended Data Table 1).

$$\mu = \begin{cases} \mu_0, & \text{for } \varepsilon_{\mathrm{pl}} \leq \varepsilon_0 \\ \mu_0 \cdot \dfrac{\varepsilon_{\mathrm{pl}} - \varepsilon_0}{\varepsilon_1 - \varepsilon_0}, & \text{for } \varepsilon_0 < \varepsilon_{\mathrm{pl}} < \varepsilon_1 \\ \mu_1, & \text{for } \varepsilon_{\mathrm{pl}} \geq \varepsilon_1 \end{cases}$$

Surface process model

For the surface processes in our model, we use the Finite Difference Surface Process Model (FDSPM), which is fully coupled to the thermo-mechanical part of the code as described in earlier works[3]. This code takes into account hillslope diffusion, erosion, sedimentation, and advective transport of the topographic surface h. Sediments formed through erosion are transported into forming basins in a *mass-conservative* manner, which most other surface process models do not. This is critical for regional geodynamic studies. The surface evolves following the governing equation

$$\frac{\partial h}{\partial t} + u_H \cdot \nabla_H \mathrm{h} = u_V + \nabla_H \cdot \left(\kappa(\boldsymbol{x})\right)\nabla_H \mathrm{h}$$

Where u_H is the horizontal velocity field (u_x, u_z), $\kappa(\boldsymbol{x})$ denotes the diffusivity depending on position $\boldsymbol{x}$ (x, y, z). However, here we assume a constant diffusivity κ_c across the surface domain, yielding

$$\frac{\partial h}{\partial t} + u_H \cdot \nabla_H h = u_V + \kappa_c \nabla_H^2 h$$

Where the topographic curvature is denoted with $\nabla_H^2 h$. Erosion takes place when the curvature is negative, while sedimentation occurs when it is positive. The governing equation is solved using a first-order operator-splitting approach which involves calculating the advective and diffusive terms sequentially[3].

Sticky air topography correction

In our model setup, we use a 20 km thick layer of sticky air on top of the plates. In any such model, volume is conserved by prescribing outflux of air at the top and asthenosphere at the bottom that compensates exactly for the incoming amounts of air and "rock" units. Therefore, the volume of sticky air is constant. Mountain ranges and plateaus take up some of the "sticky atmosphere", causing the air to press down on the hinterland, potentially causing subsidence. One can estimate this effect as follows:

$$H_{\text{mountains}} \cdot f_{\text{mountains}} \cdot L_x \cdot L_z + y_{\text{hinterland}} * (1 - f_{\text{mountains}}) * L_x \cdot L_z = y_{\text{air}} \cdot L_x \cdot L_z$$

Where L_x and L_z are model x and z dimensions, $f_{\text{mountains}}$ is the fraction of the surface that is occupied by positive topography. Reorganising and simplifying yields

$$y_{\text{hinterland}} = y_{\text{air}} - \frac{H_{\text{mountains}} \cdot f_{\text{mountains}}}{1 - f_{\text{mountains}}}$$

relative to the y-coordinate of initial crust-air interface, or

$$H_{\text{hinterland}} = -\frac{H_{\text{mountains}} \cdot f_{\text{mountains}}}{1 - f_{\text{mountains}}}$$

relative to the interface itself. This effect is relatively small if topography builds in a small portion of the available space. A 500 km 100 km wide orogen in a model domain like ours means ~420 m subsidence.

However, for an average height of 5 km in about half the model XZ domain, the average air-induced subsidence in the hinterland is 5 km, which corresponds well to the "background" topographic curve from a point in the undeformed hinterland.

The topography in Fig. 2 in the main document and in Extended Data Fig. 5 was corrected for subsidence induced by the constant volume of sticky air, such that the topography near the south-eastern model boundary is zero.

Supplementary bibliography

1. Gerya, T. V. & Yuen, D. A. Characteristics-based marker-in-cell method with conservative finite-differences schemes for modeling geological flows with strongly variable transport properties. *Phys. Earth Planet. Inter.* **140**, 293–318 (2003).
2. Gerya, T. V. *Introduction to Numerical Geodynamic Modelling*. (Cambridge University Press, 2019). doi:10.1017/9781316534243.
3. Munch, J., Ueda, K., Schnydrig, S., May, D. A. & Gerya, T. V. Contrasting influence of sediments vs surface processes on retreating subduction zones dynamics. *Tectonophysics* **836**, 229410 (2022).
4. Burg, J.-P. & Gerya, T. The role of viscous heating in Barrovian metamorphism of collisional orogens: thermomechanical models and application to the Lepontine Dome in the Central Alps. *J. Metamorph. Geol.* **23**, 75–95 (2005).
5. Chen, L. & Gerya, T. V. The role of lateral lithospheric strength heterogeneities in orogenic plateau growth: Insights from 3-D thermo-mechanical modeling. *J. Geophys. Res. Solid Earth* **121**, 3118–3138 (2016).
6. Chen, L., Capitanio, F. A., Liu, L. & Gerya, T. V. Crustal rheology controls on the Tibetan plateau formation during India-Asia convergence. *Nat. Commun.* **8**, 15992 (2017).
7. Ranalli, G. *Rheology of the Earth*. (Springer Science & Business Media, 1995).
8. Hirth, G. & Kohlstedt, D. Rheology of the upper mantle and the mantle wedge: A view from the experimentalists. in *Geophysical Monograph Series* (ed. Eiler, J.) vol. 138 83–105 (American Geophysical Union, Washington, D. C., 2003).

9. Karato, S. & Wu, P. Rheology of the Upper Mantle: A Synthesis. *Science* **260**, 771–778 (1993).
10. Schierjott, J. C., Thielmann, M., Rozel, A. B., Golabek, G. J. & Gerya, T. V. Can Grain Size Reduction Initiate Transform Faults?—Insights From a 3-D Numerical Study. *Tectonics* **39**, e2019TC005793 (2020).

Supplementary Video:

Extended Data Video 1: https://youtu.be/KJVqdtfFxzM

Description:

Top panel: North is to the left. Two slices at x = 100 and x = 500 km showing rock composition. Crust and sediments are opaque, mantle is made transparent. A contour of the crust-mantle interface (Moho) is shown, with its depth projected on it. The velocity of the **upper** crust is shown to highlight its escape flow towards the east. Bottom panels: Top view showing the model surface, plotting the topography and uplift rates. This topography is not corrected for the background subsidence described in the Methods section.

Main model stages are annotated: Stage A: Initial deformation, mountain building Stage B: Proto-syntaxis formation in the corner Stage C: Plateau growth, fast ductile crustal channel flow around the corner, slab flattening Stage D: Syntaxis widening, slower crustal flow, and plateau collapse.

Supplementary Figures

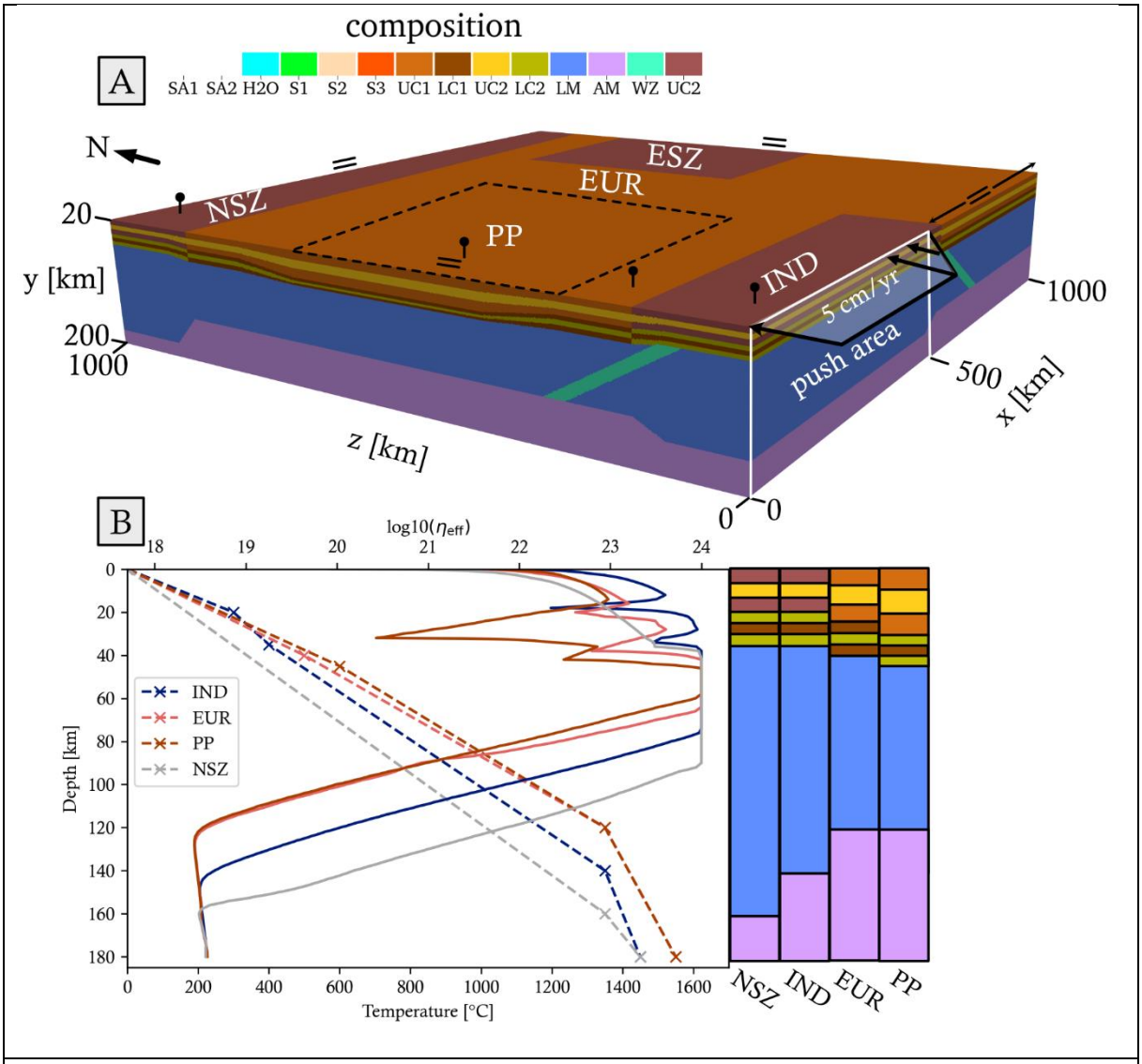

Extended Data Figure 1 | Reference model setup. Initial setup of the reference model showing the plate configuration and kinematic boundary conditions in panel A. Panel B depicts the rheological contrasts obtained by imposing different crustal thicknesses and initial geothermal profiles. Upper and lower crust have sublayers with otherwise identical properties (Extended Data Table 1). Pins in panel A indicate locations of effective viscosity profiles taken in an early timestep. The proto-plateau is the weakest unit due its thick, warm upper crust. IND indenting "Indian" plate; EUR "Eurasian" plate; PP - Proto-plateau, NSZ – Northern strong zone representing the Tarim basin; ESZ - Eastern Strong zone representing the Sichuan basin. SA – Sticky air; UC- Upper crust; LC – Lower crust; LM – Lithospheric mantle; AM – Asthenospheric mantle; WZ – Weak zone.

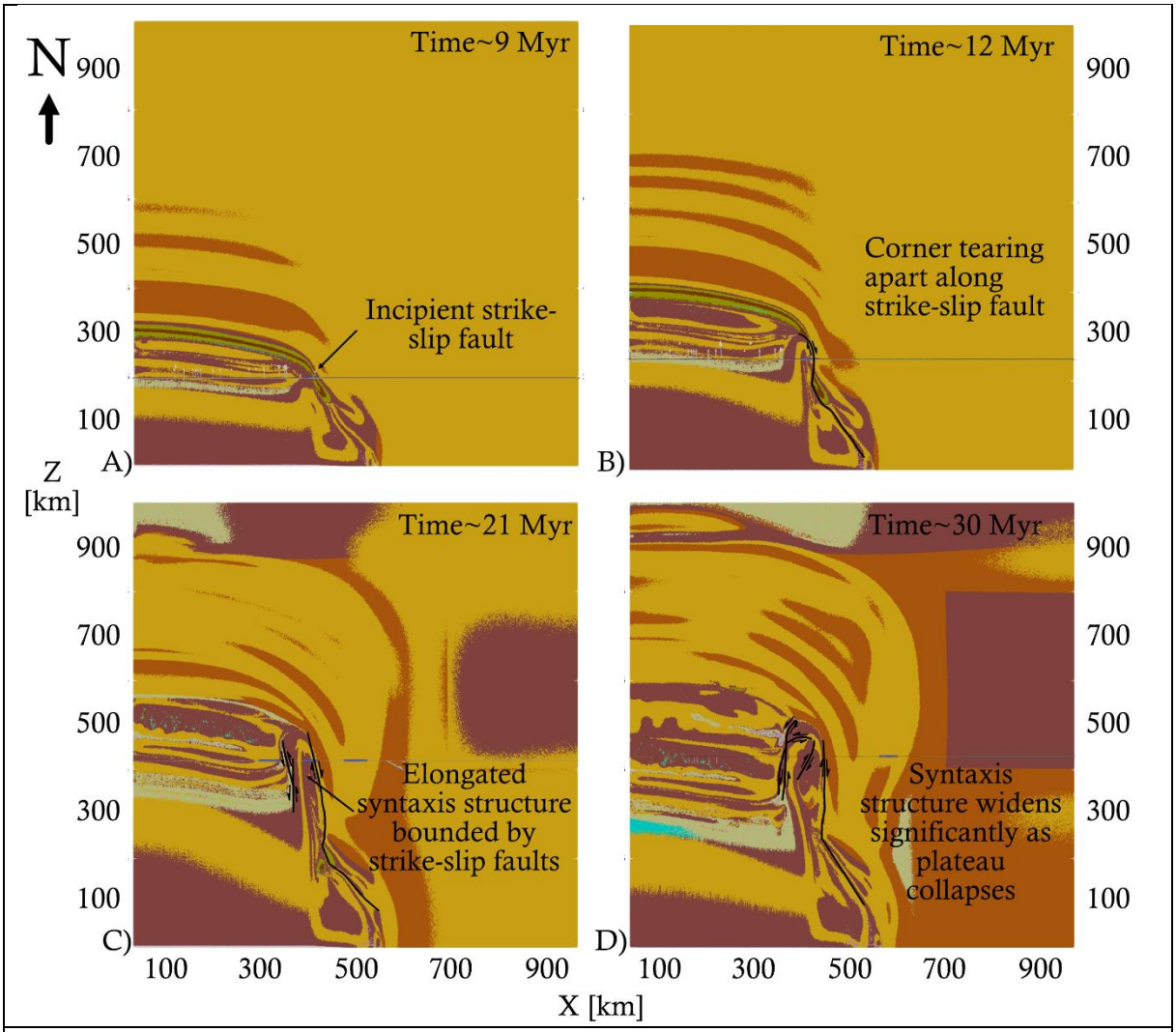

Extended Data Figure 2 | Development of strike-slip faults in the reference model syntaxis. Horizontal slices of rock composition at Y = 35 km with strike-slip faults in the continental corner indicated. The EW slices through the syntaxis whose outlines are visible here can be seen in Fig. 2 in the main document. The syntaxis structure undergoes significant elongation before it starts to widen. Its northeastern edge is coupled to the plateau corner, while its southwestern side is coupled more to the pro-wedge of the mountain range.

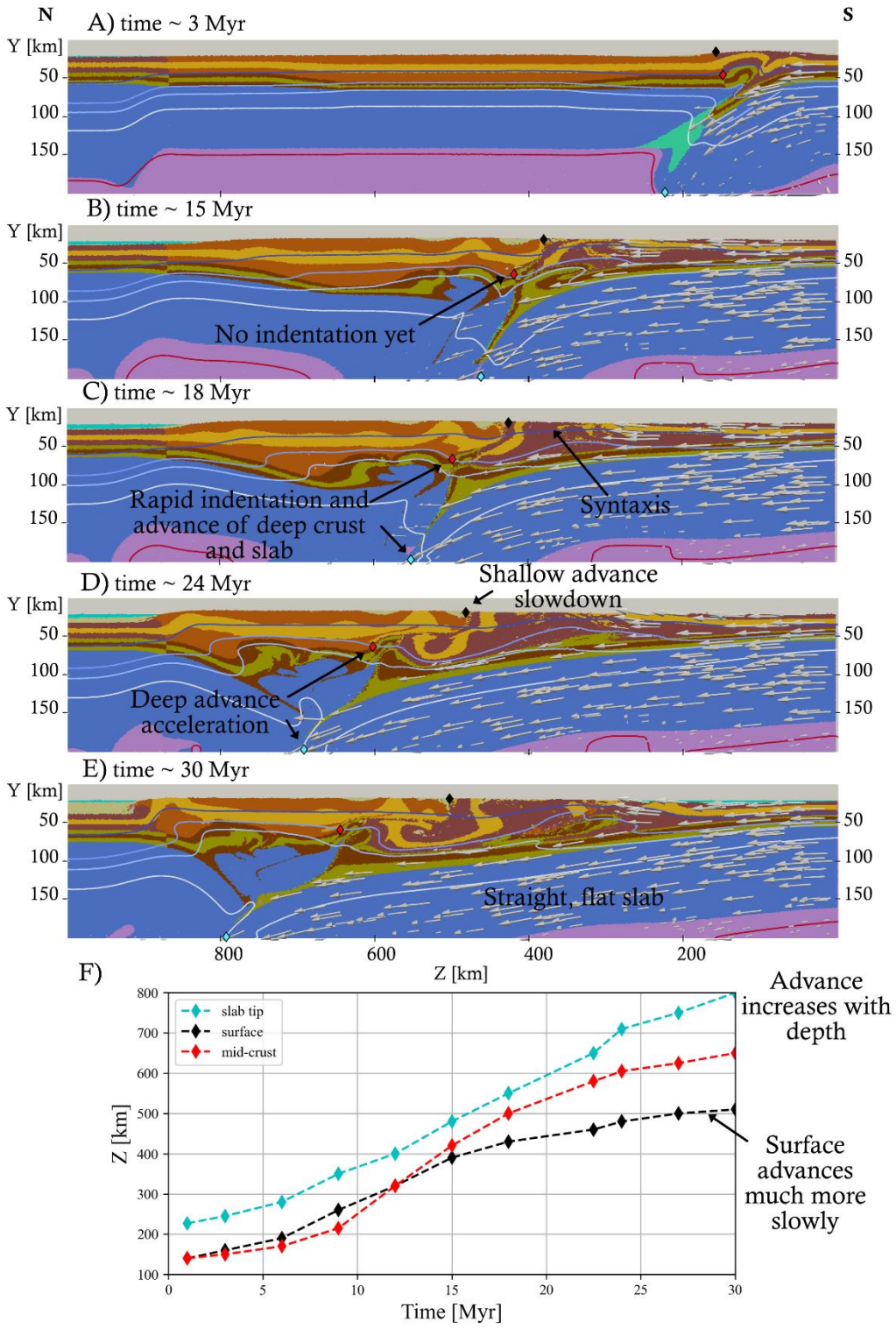

Extended Data Figure 3 | Advance of plate boundary differs with depth. A-E) Evolution of the convergence-parallel position of the IND-EUR plate boundary at the surface, the upper/lower crust interface, and the indenter slab tip at the X = 400 km slice. North is to the left. The respective locations were tracked manually. Overview in panel F. There is a clear decoupling occurring following syntaxis formation, which is mostly a crustal process. The lower crust and mantle lithosphere of the indenter advance over 250 km further north than the upper crust. Compare with Figure 4 in the main text, where horizontal velocity is averaged for all crustal markers from Z = 500 km onward.

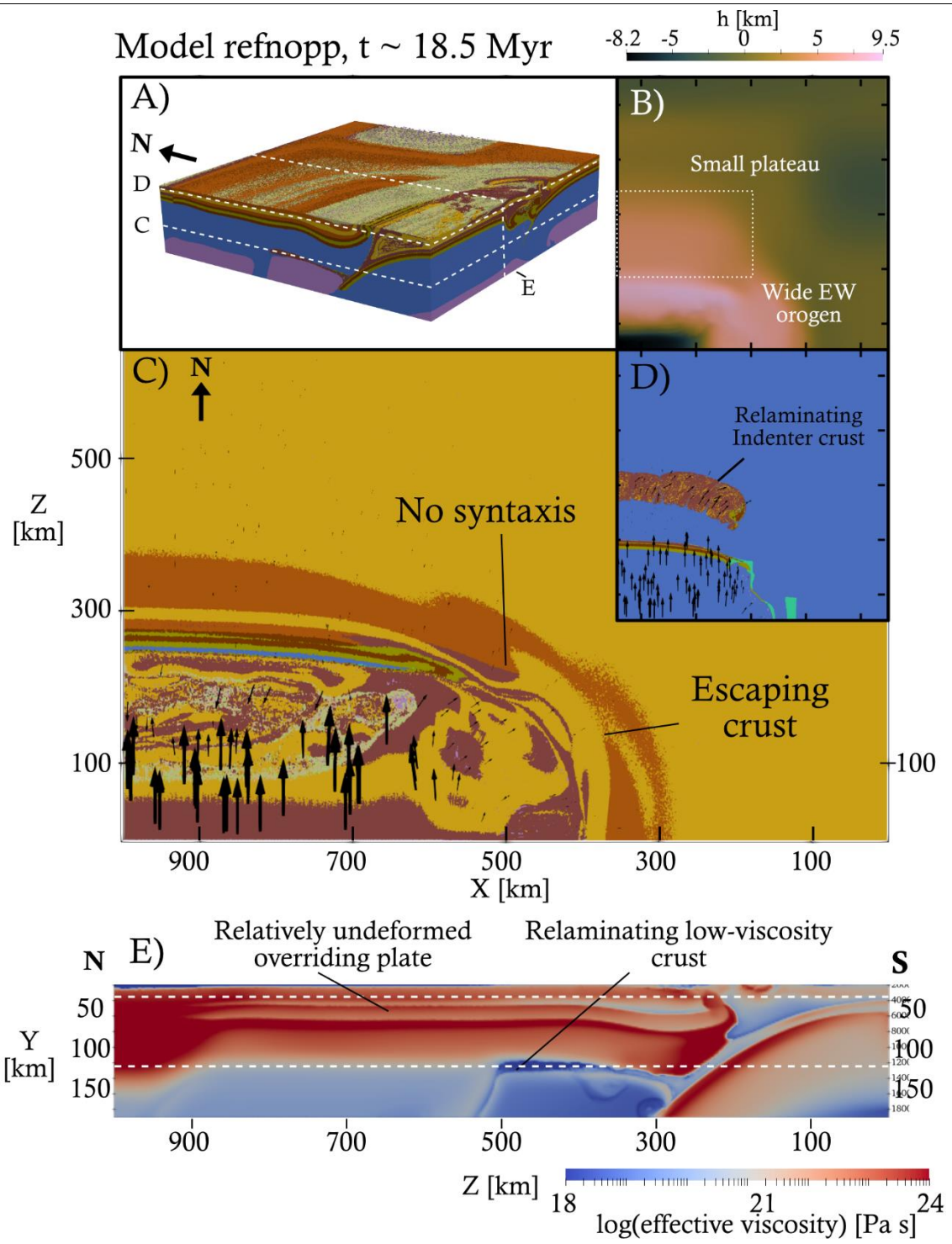

Extended Data Figure 4 | No syntaxis formation when excluding the proto-plateau. Overview figure illustrating arguments as to why no syntaxis develops without the proto-plateau. Panel A shows the oblique composition with the outermost 100 km cut away. Locations are indicated of horizontal slices at Y = 35 km (panel C) and 125 km (panel D) and a vertical viscosity slice through X = 400 km (panel E). The resistance of the hinterland against shortening stagnates northward subduction and indentation, hampering plateau growth and channel formation. Some subducted indenter crust relaminates underneath the "Eurasian" plate. Convergence is accommodated by northward subduction and eastward shortening in ***front*** of the corner. Almost no convergence is accommodated by the hinterland.

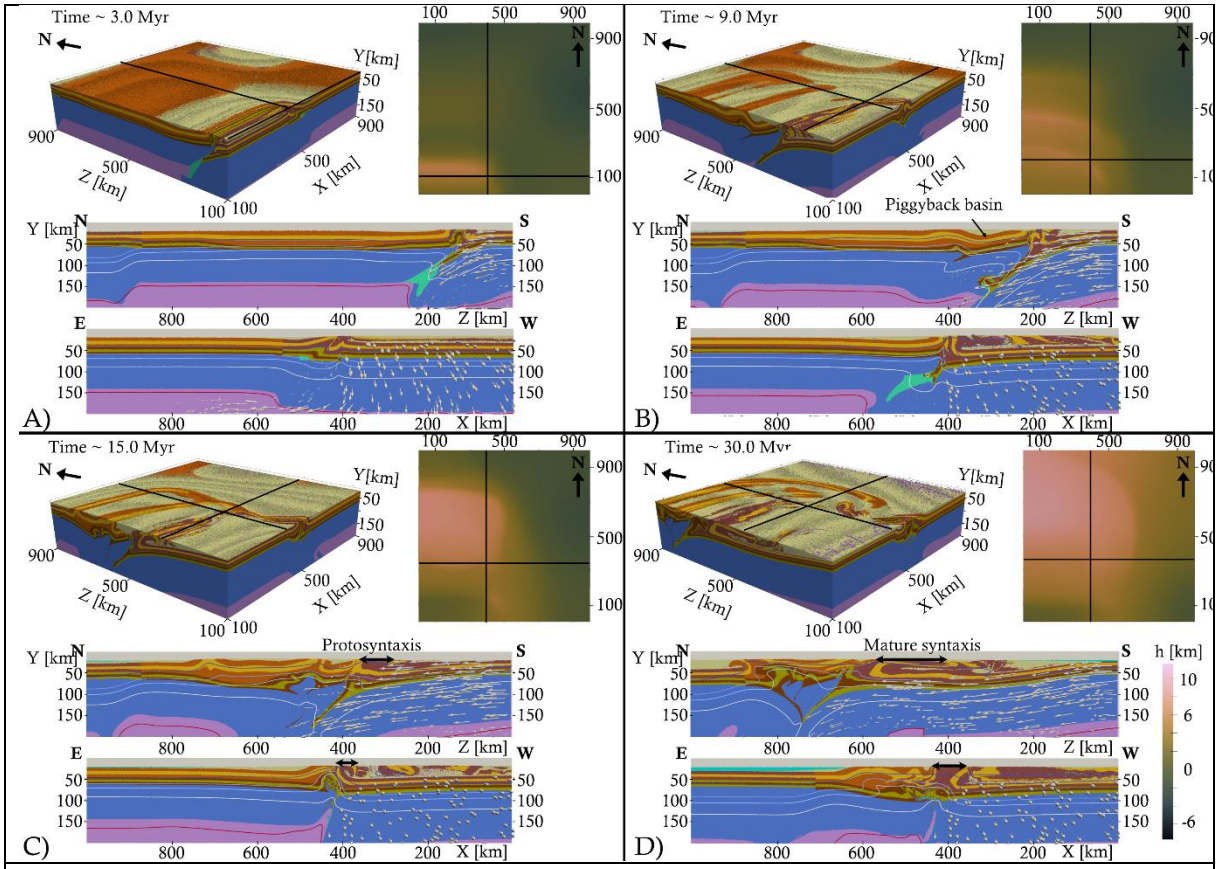

Extended Data Figure 5| Syntaxis development under high erosion conditions. Similar visualisation as Fig. 3 in the main manuscript. There are significant differences in the structure of e.g. the pro-wedge and the localisation of strike-slip faults. Nevertheless, the main patterns hold and a syntaxis still forms. The final crustal thickness of the plateau is ~20 km less than in the reference model.

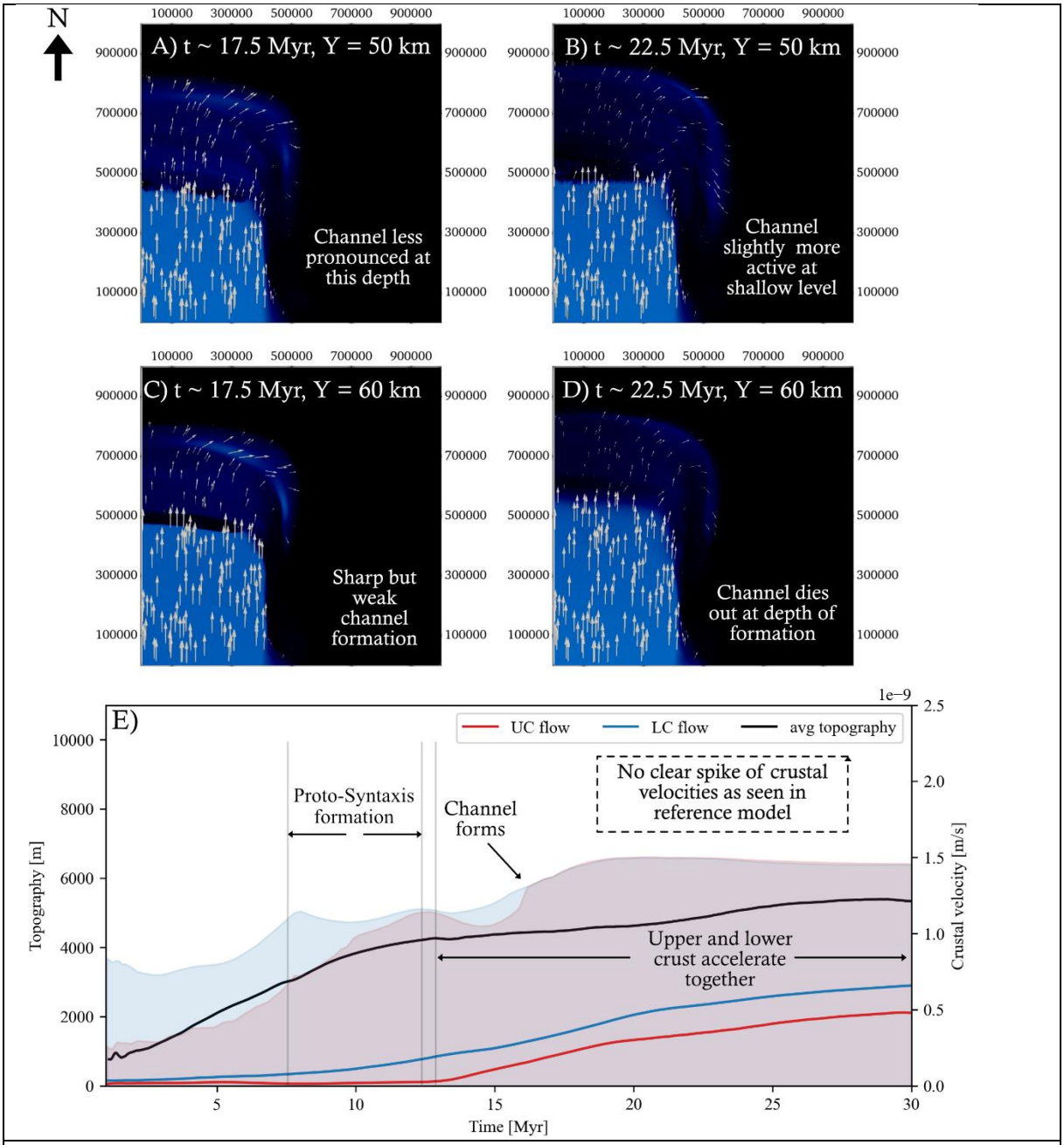

Extended Data Figure 6 | Channel shallowing and syntaxis uplift vs crustal flow for strong erosion model. A-D) Horizontal depth slices at Y = 50 and Y = 60 km showing the horizontal velocity similar to Fig. 3 in the main text. E) Same plot as in Figure 4 in the main text, but for the high erosion model. The most notable differences are a lower final topography, and the lack of a spike of crustal velocities after channel formation.

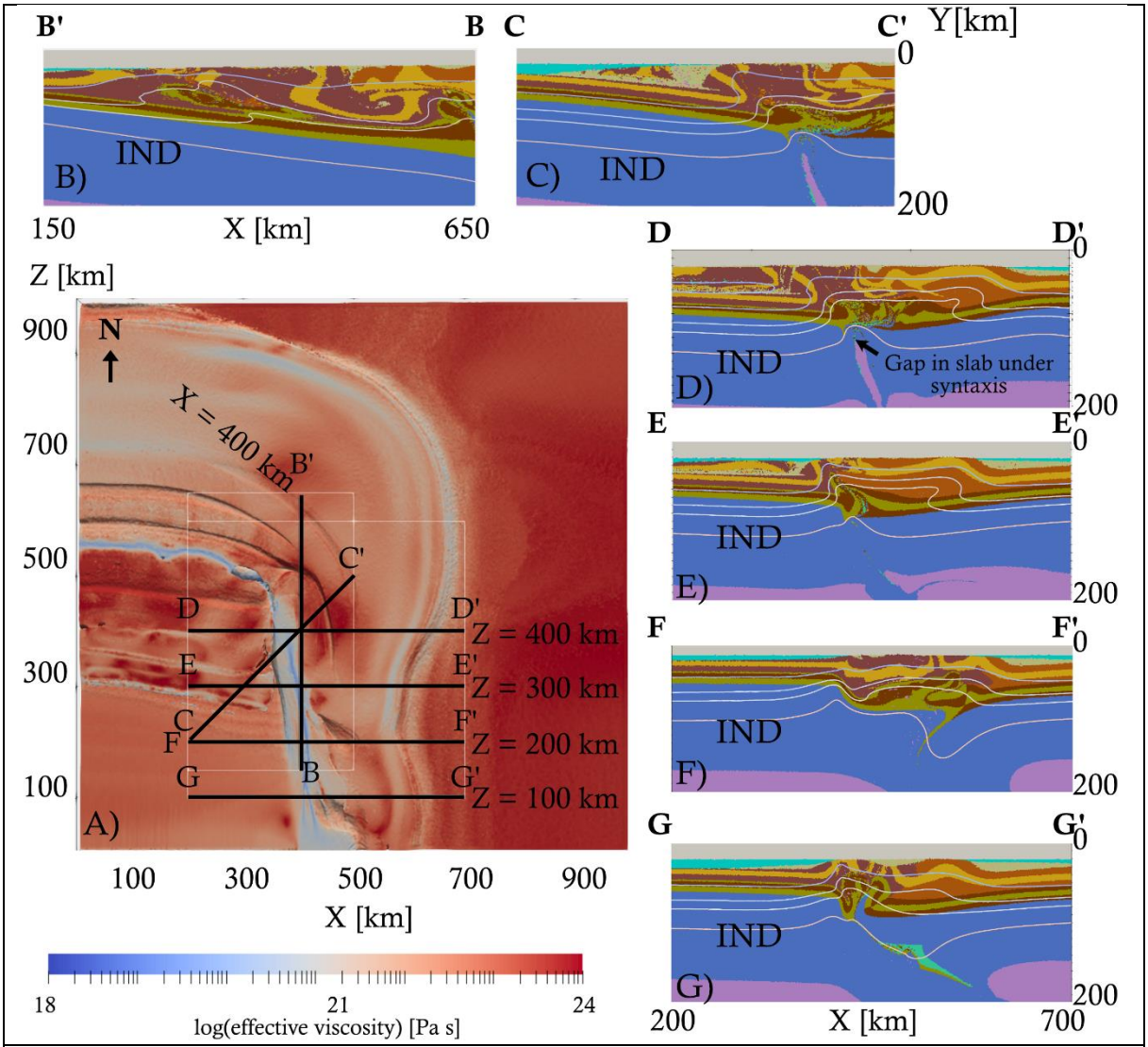

Extended Data Figure 7 | Indian slab geometry under the syntaxis. A) An iso-density contour (2650 kg/m^3, upper crust) shows the syntaxis in the middle. Sections through two different subsets of the composition field (outlined in white) show the slab geometry under the syntaxis. one NS-cross-section (B), one SW-NE cross-section (C) and four E-W cross-sections (D-G) depicting composition overlain with temperature contours (300, 500, 600 and 800°C) show that eastward subduction is less well developed towards the north compared to the south.